Growth of a black hole in a scalar field cosmology

Jake Doherty, Miguel Gracia-Linares, and Pablo Laguna
Center of Gravitational Physics, Department of Physics, University of Texas at Austin, Austin, Texas 78712, USA

(Received 30 April 2025; accepted 26 July 2025; published 14 August 2025)

We present a numerical relativity study of the accretion properties of a nonspinning black hole in a cosmology driven by a scalar field. The simulations are carried out with a modified moving-puncture gauge condition suitable for cosmological space-times. We considered a scalar field with potential $V = \lambda\varphi^4/4$ and derived the black hole mass growth formula for this scenario using the dynamical horizon framework. As with perturbative studies, we find that the accretion rate $\dot{M} \propto M^2$, with M the mass of the black hole, and that $\dot{M} \propto \dot{\varphi}^2$. We verify that the results of the simulations satisfy the mass growth formula. Unexpectedly, the scalar field dynamics in the neighborhood of the black hole is not significantly different from the behavior of the field far away from the hole. We found situations where the black hole can grow ∼15% of its initial mass before the scalar field reaches the bottom of its potential.

DOI: 10.1103/nypy-cd2f

I. INTRODUCTION

With the current sensitivity of the gravitational wave (GW) detectors, observations of binary black hole (BBH) mergers by the LIGO, Virgo, and KAGRA (LVK) Collaboration [1–4] show consistency with the assumption that general relativity (GR) is the correct theory of gravity and that the environment in which the systems merge is in a vacuum. As the sensitivity of the detectors improves, GW observations will present us with a unique opportunity to uncover phenomena that could be governed by alternatives to GR and the Standard Model of particle physics. The possibility that GW observations could help us decipher the nature of dark matter and dark energy is also not far-fetched. At the very least, GWs will help us to identify the properties of the environments hosting sources of gravitational radiation [5,6]. Several studies have addressed finding evidence for modified theories of gravity [4,7,8] or physics beyond the Standard Model, e.g., ultralight bosons [9,10]. For massive black holes BHs, in astrophysical scenarios in which gravitational radiation is accompanied with electromagnetic radiation, the presence of gas/dust cannot be ignored; examples are active galactic nuclei [11–17] or accretion disks [18–20]. BH accretion is expected to influence the coalescence and translate into intensity variations in the GWs emitted [21–25] and also affect the final BH characteristics, including the gravitational recoil [26].

Several studies have examined the impact of a scalar field environment in the GW emission of compact mergers. These include phenomenological studies about environmental signatures on isolated BHs or extreme mass ratio inspirals [19,27], binaries in various modified gravity theories [28–33] or within axion fields [34], scalar field dynamics in BH space-times [35,36] and their phenomena, such as superradiance [37–40] and scalarization [39,41], scalar dynamics in the transition from inspiraling BHs to a single perturbed BH [42], scalar radiation from BBH systems [43,44], BBH mergers in $f(R)$ theories [45] and in dynamical Chern-Simons gravity [46], effects of axion-like scalar field environment on BBH mergers [47], BBH dynamics in Einstein-Maxwell-dilation theory [48], and in scalar Gauss-Bonnet gravity [49]. These studies were partially motivated by the possibility of scalar fields to explain the nature of dark matter [50] or for scalar-tensor and $f(R)$ theories of gravity [51–53].

Generally, there are two processes by which a scalar field environment impacts the BBH dynamics. One is accretion. As the BHs grow, the evolution of the orbital frequency (and therefore that of the emitted GWs) is altered relative to the vacuum case. Also, the mass of the final BH is larger than that of the corresponding BH in vacuum, impacting its ringdown structure and the excitation of ringdown modes. This would be particularly important for massive binaries, for which the ringdown of the final BH dominates the signal inside the detector's band. In this case, environmental effects could be detectable through the ringdown structure [54,55]. The second effect is dissipation or dragging. As the BHs interact with the scalar field environment, they experience dynamical friction [56,57].

Without a potential, a BBH in a homogeneous and initially stationary sea of scalar field will behave exactly as in a vacuum. This can be seen from $G_{ab} = 8\pi T_{ab}$ with $T_{ab} = \nabla_a\varphi\nabla_b\varphi - g_{ab}(\nabla_c\varphi\nabla^c\varphi/2 + V)$ and $\nabla^a\nabla_a\varphi = V_{,\varphi}$. If $V = 0$, and initially $\varphi =$ constant and $\partial_t\varphi = 0$, we get that $G_{ab} = 0$. Thus, a dynamical scalar field is needed to get differences from BBH inspirals and mergers in a vacuum. One can achieve this with an inhomogeneous field, a nonstationary field, or a scalar field potential. Our previous work used an inhomogeneous field (bubble encapsulating the binary) with and without a vanishing potential [26,58]. The reason for using a bubble was to have an asymptotically flat space-time and a vacuum in the neighborhood of the binary.

We propose triggering scalar field dynamics with a potential. To avoid the complexities associated with the zoo of inflationary potential, we will consider a $V = \lambda\varphi^4/4$ potential, so the only knob to turn is the parameter λ. In the present work, we will study a single, nonrotating BH. The first step will be to derive a BH growth formula, and the second will be to check the correctness of the formula with numerical relativity simulations. Studies exist investigating accretion of scalar fields by BHs. Scalar field BH accretion has been investigated under both slow-roll and ultraslow-roll approximations through a perturbative expansion of the Einstein equations [59,60]. Also, approximate analytical solutions for a dynamical spherically symmetric black hole in the presence of a minimally coupled self-interacting scalar field have been derived [61]. Our study does not make any approximations; we solve the full nonlinear set of GR equations. In Refs. [59,61,62], it was found that the growth rate of the BH was proportional to the square of its mass, $\dot{M} \propto M^2$, bearing a similar resemblance to the standard Bondi accretion rate. On the other hand, in a study investigating a BH in a scalar field cosmology, Ref. [63] found a growth rate $\dot{M} \propto M^3$. As in [59,61], we find that $\dot{M} \propto \dot{\varphi}^2$.

The paper is organized as follows: A summary of the method to construct initial data of a BH in the presence of a dynamical cosmological background driven by a scalar field is presented in Sec. II. Evolution equations for the scalar field and gauge conditions are discussed in Sec. III. Numerical setup and simulation parameters are given in Sec. IV. Scalar field evolution results are discussed in Sec. V. Results showing how the dynamics of the system obey the area increase law are presented in Sec. VI. BH mass growth is discussed in Sec. VII. Conclusions are given in Sec. VIII. Quantities are reported in units of the puncture mass m of the BH, with $G = c = 1$. Space-time signature is $(-+++)$. Space-time indices are denoted with Latin letters from the beginning of the alphabet. Spatial tensor indices are denoted with Latin letters from the middle of the alphabet. Also, $()^{\cdot} \equiv d/dt$, and $()^{\circ} \equiv d/d\tau$ with t and τ as coordinate and proper time, respectively.

II. INITIAL DATA

Under the $3+1$ decomposition of the Einstein field equations [64], a space-time with a metric g_{ab} is foliated by spacelike hypersurfaces Σ with unit timelike normals n^a. The initial data consist of the spatial metric γ_{ab} intrinsic to Σ, the extrinsic curvature K_{ab} of Σ, the energy density ρ, and the momentum density S_a. These quantities are obtained from

$$\gamma_{ab} = g_{ab} + n_a n_b, \tag{1}$$

$$K_{ab} = -\frac{1}{2}\mathcal{L}_n\gamma_{ab} = -\gamma_a{}^c\gamma_b{}^d\nabla_c n_d, \tag{2}$$

$$\rho = n^a n^b T_{ab}, \tag{3}$$

$$S^a = -\gamma^{ab} n^c T_{bc}, \tag{4}$$

with ∇ covariant differentiation with respect to g_{ab} and T^{ab} the stress-energy tensor. For our case of a scalar field φ, the stress-energy tensor T_{ab} has the form

$$T_{ab} = \nabla_a\varphi\nabla_b\varphi - g_{ab}\left(\frac{1}{2}\nabla_c\varphi\nabla^c\varphi + V\right). \tag{5}$$

Therefore,

$$\rho = \frac{1}{2}\Pi^2 + \frac{1}{2}D^i\varphi D_i\varphi + V, \tag{6}$$

$$S_i = -\Pi D_i\varphi, \tag{7}$$

where $\Pi \equiv -n^a\nabla_a\varphi$ is the conjugate momentum of φ and V is its potential. As mentioned before, we set $V = \lambda\varphi^4/4$. The operator D_i denotes covariant differentiation associated with γ_{ij}.

The initial data must satisfy the Hamiltonian and momentum constraint equations. Namely,

$$\mathcal{R} + K^2 - K_{ij}K^{ij} = 16\pi\rho, \tag{8}$$

$$D_j K^{ij} - D^i K = 8\pi S^i, \tag{9}$$

respectively. Here, $\mathcal{R}$ is the Ricci scalar in Σ and K is the trace of K_{ij}.

We solve the constraints (8) and (9) following the York-Lichnerowicz conformal approach [65–68] in which

$$\gamma_{ij} = \psi^4\tilde{\gamma}_{ij}, \tag{10}$$

$$A_{ij} = \psi^{-2}\tilde{A}_{ij}, \tag{11}$$

where A_{ij} is the traceless part of the extrinsic curvature. In addition, we introduce $\tilde{\Pi} = \psi^6\Pi$. With these transformations, the Hamiltonian (8) and the momentum (9) constraints read, respectively,

$$\tilde{\Delta}\psi - \left(\frac{1}{8}\tilde{\mathcal{R}} - \pi\tilde{D}^i\phi\tilde{D}_i\phi\right)\psi - \left(\frac{1}{12}K^2 - 2\pi V\right)\psi^5 + \left(\frac{1}{8}\tilde{A}^{ij}\tilde{A}_{ij} + \pi\tilde{\Pi}^2\right)\psi^{-7} = 0, \tag{12}$$

$$\tilde{D}_j\tilde{A}^{ji} - \frac{2}{3}\psi^6\tilde{D}^iK = -8\pi\tilde{\Pi}\tilde{D}^i\phi, \tag{13}$$

where $\tilde{\mathcal{R}}$ is the Ricci scalar of the conformal space, $\tilde{D}_i$ denotes covariant differentiation associated with the conformal metric $\tilde{\gamma}_{ij}$, and $\tilde{\Delta} \equiv \tilde{D}_i\tilde{D}^i$. For simplicity, we also set the conformal space to be flat, i.e., $\tilde{\gamma}_{ij} = \eta_{ij}$. Thus, the Hamiltonian and the momentum constraints become

$$\partial^j\partial_j\psi + \pi\psi\partial^j\phi\partial_j\phi - \left(\frac{1}{12}K^2 - 2\pi V\right)\psi^5 + \left(\frac{1}{8}\tilde{A}^{ij}\tilde{A}_{ij} + \pi\tilde{\Pi}^2\right)\psi^{-7} = 0, \tag{14}$$

$$\partial_j\tilde{A}^{ji} - \frac{2}{3}\psi^6\partial^iK = -8\pi\tilde{\Pi}\partial^i\phi. \tag{15}$$

Because our system involves a BH, we will model the hole as a puncture where the conformal factor has the form

$$\psi = 1 + \frac{m}{2r} + u, \tag{16}$$

with m as the puncture bare mass parameter. If the BH has momentum or spin, we will be using the Bowen-York solutions [69] $\tilde{A}^{ji}$ of the momentum constraint in which $\partial_j\tilde{A}^{ji} = 0$. To use these solutions, we must choose K, φ, and Π so that the terms involving these quantities in Eq. (15) vanish. We accomplish this by setting $\Pi = 0$, $K = \text{constant}$, and $\varphi = \text{constant}$, which implies $\dot{\varphi} = 0$. With these assumptions, Eq. (14) takes the following form:

$$\partial^j\partial_j\psi + \frac{1}{8}\tilde{A}^{ij}\tilde{A}_{ij}\psi^{-7} - \left(\frac{1}{12}K^2 - 2\pi V\right)\psi^5 = 0. \tag{17}$$

The last term in this equation will diverge at the puncture location because of the form of the conformal factor (16). To avoid this, we set $K^2 = 24\pi V$. Notice that, in a homogeneous cosmological setup, $K = -3H$, and this equation becomes $H^2 = 8\pi V/3$, the Friedmann equation for a cosmology driven by a scalar field at the initial time when $\dot{\varphi} = 0$. Therefore, we need to solve the equation

$$\partial^j\partial_j\psi + \frac{1}{8}\tilde{A}^{ij}\tilde{A}_{ij}\psi^{-7} = 0, \tag{18}$$

which is the equation commonly solved for vacuum space-times for a BH modeled by punctures.

Since we are focusing on a single, nonspinning BH without linear momentum, $\tilde{A}^{ij} = 0$, and the solution to Eq. (17) is Eq. (16) with $u = 0$. In a vacuum space-time, the bare mass parameter would be the mass of the BH. In our case, this is not the case due to the scalar field φ. The mass M of the BH would be obtained from the area A of its apparent horizon as $M = R/2 = \sqrt{A/16\pi}$ with R the areal radius of the BH.

III. EVOLUTION EQUATIONS AND GAUGE CONDITIONS

We solve the Einstein equations using the Baumgarte-Shapiro-Shibata-Nakamura (BSSN) formulation [64,70,71]. The evolution equation for the scalar field is $\nabla^a\nabla_a\varphi = V_{,\varphi}$. We decompose this equation into a $3+1$ form with the help of the spatial metric γ_{ab} and the unit normal $n^a = (1, -\beta^i)/\alpha$, where α is the lapse function and β^i is the shift vector. The equation of motion takes the form

$$\partial_t\varphi - \beta^i\partial_i\varphi = -\alpha\Pi, \tag{19}$$

$$\partial_t\Pi - \beta^i\partial_i\Pi = -\alpha D^iD_i\varphi - D^i\alpha D_i\varphi + \alpha K\Pi + \alpha V_{,\varphi}. \tag{20}$$

For the evolution, we used a modified version of the moving-puncture gauge [72,73] to evolve α and β^i. The moving-puncture gauge commonly used for BHs in vacuum is

$$(\partial_t - \beta^j\partial_i)\alpha = -2\alpha K, \tag{21}$$

$$\partial_t\beta^i = \frac{3}{4}B^i, \tag{22}$$

$$\partial_tB^i = \partial_t\bar{\Gamma}^i - \eta B^i, \tag{23}$$

where η is a parameter and $\bar{\Gamma}^i \equiv -\partial_j\bar{\gamma}^{ij}$ with $\bar{\gamma}_{ij} = \chi^4\gamma_{ij}$ as the conformal metric in the BSSN system of equations [64,70,71]. Far away from the BHs, where asymptotic flatness holds, the moving-puncture gauge is consistent with $\alpha = 1$, $\beta^i = 0$, and $\gamma_{ij} = \eta_{ij}$.

In the absence of the BH, our space-time is that of a spatially flat Friedmann-Robertson-Walker cosmology, with a metric given as

$$ds^2 = -dt^2 + a^2(t)\eta_{ij}dx^idx^j. \tag{24}$$

That is, $\alpha = 1$, $\beta^i = 0$, and $\gamma_{ij} = a^2(t)\eta_{ij}$ with the expansion factor obeying the Friedmann equation

$$H^2 = \frac{8\pi}{3}\rho = \frac{8\pi}{3}\left(\frac{1}{2}\dot{\varphi}^2 + V\right) \tag{25}$$

and φ satisfying

$$\ddot{\varphi} + 3H\dot{\varphi} = -V_{,\varphi}, \tag{26}$$

with $H \equiv \dot{a}/a$. Therefore, for our situation of a BH in an expanding cosmology, we must ensure that far away from

TABLE I. Initial scalar field configuration parameters. The initial BH mass M_0 is given in units of m.

$\bar{\lambda}$	φ_0	$\bar{V}_{,\varphi}$	M_0	φ_0	$\bar{V}_{,\varphi}$	M_0
2	0.900	1.458	1.001	0.900	1.458	1.001
4	0.900	2.916	1.002	0.714	1.458	1.002
6	0.900	4.374	1.003	0.624	1.458	1.001
8	0.900	5.832	1.004	0.567	1.458	1.001
10	0.900	7.290	1.006	0.526	1.458	1.001

the BH we approach a Friedmann-Robertson-Walker cosmology.

The moving-puncture gauge for the shift vector can be directly applicable to our case since, asymptotically, it has $\beta^i = 0$ as a solution. What needs modification is Eq. (21) for the lapse. In its current form, this equation does not yield asymptotically $\alpha = 1$ or a constant because $K = -3H \neq 0$. To get the correct asymptotic behavior for α, we introduce the following modification:

$$(\partial_t - \beta^j \partial_j)\alpha = -2\alpha(K + \sqrt{24\pi\rho}). \quad (27)$$

With this, far from the hole, the rhs of Eq. (27) will vanish because of the Friedmann equation (25). We will refer to this condition as the "cosmological moving-puncture gauge."

IV. COMPUTATIONAL SETUP AND SCALAR FIELD CONFIGURATIONS

Numerical simulations were performed with the MAYA code [74–79], our local version of the EINSTEIN TOOLKIT code [80]. All results are given in units of the puncture mass parameter m. The initial configuration is a BH embedded in a homogeneous scalar field. As evolution proceeds, the scalar field will drive a rapid expansion of space-time, eventually preventing us from numerically resolving the BH. We use 12 levels of mesh refinements in a computational box of size 120 m with a grid spacing of $m/840$ for the finest mesh. With this setup, we ensure resolving the BH throughout a few hundred m of evolution; this is enough dynamical evolution to address the questions under consideration. We also impose periodic boundary conditions. Strictly speaking, the presence of the BH breaks initially periodicity. However, the outer boundary is sufficiently far from the BH that its effects are minor, and to a good approximation, periodicity is allowed.

We considered $\bar{\lambda} = \{2, 4, 6, 8, 10\}$, where $\lambda \equiv \bar{\lambda} \times 10^{-4}\, m^{-2}$ and used two types of initial values φ_0 for the scalar field. In one case, as we vary $\bar{\lambda}$, we keep $\varphi_0 = 0.9$ constant. For the other type, we vary φ_0 and keep the initial value of $\bar{V}_{,\varphi} = \bar{\lambda}\varphi_0^3 = 1.458$ constant. The latter is to ensure that the initial "force" on the scalar field remains the same as we vary $\bar{\lambda}$. Table I shows the values for $\bar{\lambda}$ and φ_0 chosen, as well as the initial mass M_0 of the BH.

To demonstrate the ability of the cosmological moving-puncture gauge for preserving the standard homogeneous cosmological evolution away from the BH, Fig. 1 displays $\gamma^{1/6}$, $\gamma_{xx}^{1/2}$, and the expansion factor a as a function of proper time at the outer boundary along the x axis. The expansion factor a was obtained by solving the Friedmann equation (25). The panels from left to right are for $\{\bar{\lambda}, \varphi_0\} = \{4, 0.9\}$, $\{4, 0.714\}$, $\{10, 0.9\}$, and $\{10, 0.526\}$, respectively. The reason for using proper time is that the BH influences the asymptotic value of the lapse function α at the outer boundary, as seen in Fig. 2. The fact that $\gamma^{1/6} \approx \gamma_{xx}^{1/2} \approx a$ indicates that far from the BH the space-time behaves as a Friedmann-Robertson-Walker cosmology.

V. SCALAR FIELD DYNAMICS

Figure 3 shows the scalar field φ as a function of $x - x_h$ with x_h the horizon location for the case $\{\bar{\lambda}, \varphi_0\} = \{10, 0.526\}$. Later times correspond to darker tones of blue lines. Surprisingly, as seen in the left panel, the presence of the BH does not significantly modify the scalar field from homogeneity. The differences between the

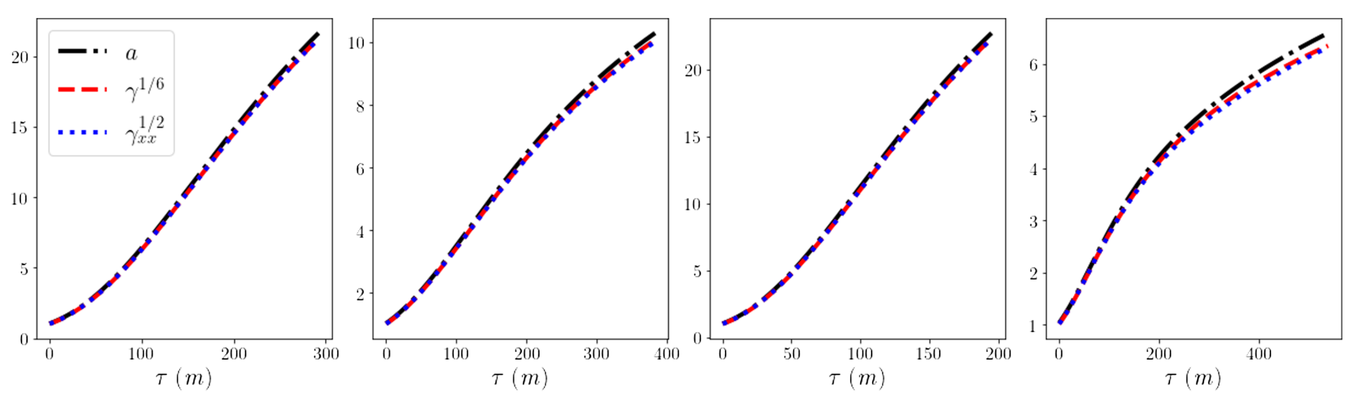

FIG. 1. $\gamma^{1/6}$, $\gamma_{xx}^{1/2}$, and a as a function of proper time and evaluated at the outer boundary in the x axis. From left to right, $\{\bar{\lambda}, \varphi_0\} = \{4, 0.9\}$, $\{4, 0.714\}$, $\{10, 0.9\}$, and $\{10, 0.526\}$, respectively.

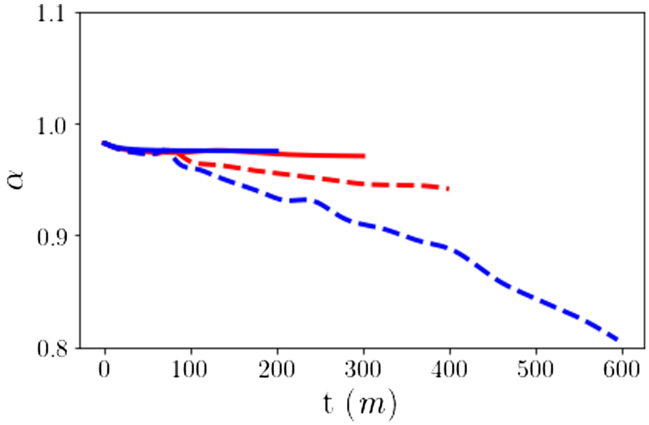

FIG. 2. Lapse function α as a function of time and evaluated at the outer boundary in the x axis. The lines correspond to $\{\bar{\lambda}, \varphi_0\} = \{4, 0.9\}$ (red, solid), $\{4, 0.714\}$ (red, dashed), $\{10, 0.9\}$ (blue, solid), and $\{10, 0.526\}$ (blue, dashed).

values at the BH horizon and the outer boundary are small, as can be seen in the right panel, where we subtract the value at the horizon. As expected, the scalar field decreases in time as it rolls down the potential. However, the decrease on the horizon is slower than far from the hole. This is related to the gravitational redshift near the hole. To help clarify this point, Fig. 4 shows the evolution of φ at the outer boundary in the first and third panels and at the horizon in the second and fourth panels. The first two panels are for the $\varphi_0 = 0.9$ cases and the last two panels are for the $\bar{V}_{,\varphi} = 1.458$ cases. Dashed lines are the values of φ from solving Eqs. (25) and (26). As expected, the larger the value of λ, the more rapidly the scalar field evolves toward the bottom of the potential. As noted above, what is remarkable is the similarity of the behavior between the values at the outer boundary and those at the horizon. To stress the difference with the homogeneous cosmological solution, in Fig. 5, we plot the same results but as a function

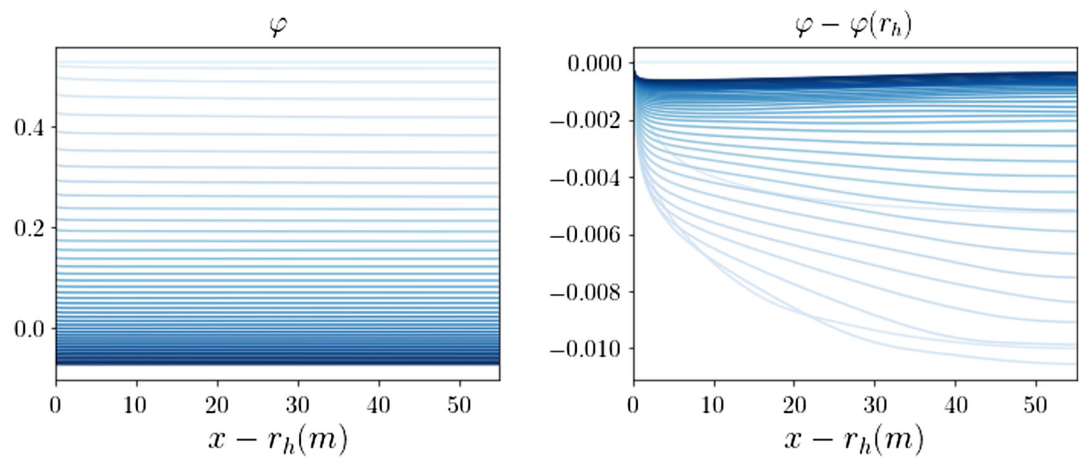

FIG. 3. Scalar field at different times as a function of $x - x_h$ with x_h the horizon location for the case $\{\bar{\lambda}, \varphi_0\} = \{10, 0.526\}$. Later times correspond to darker tones of blue in the lines. The right panel is identical to the left one, except that the scalar field at the BH horizon is shifted to zero.

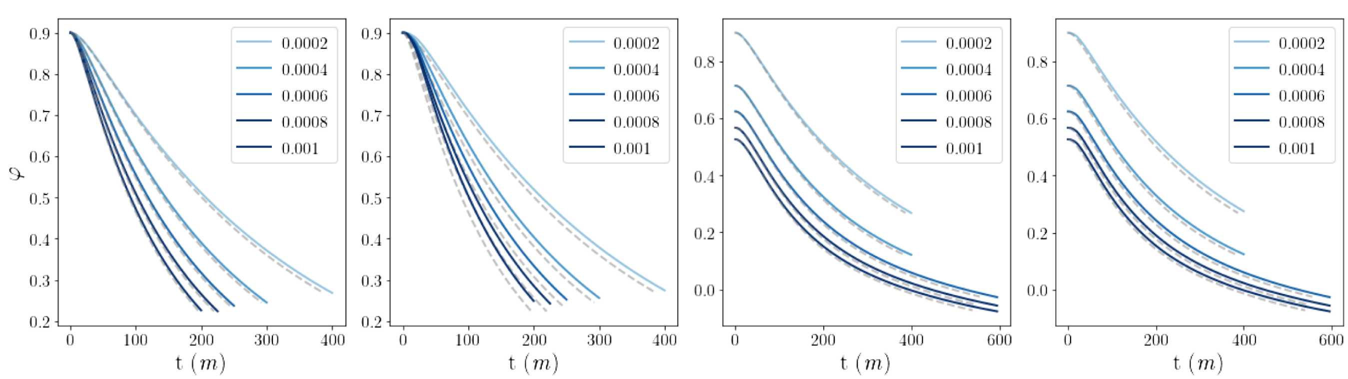

FIG. 4. Evolution of φ at the outer boundary in the first and third panels and at the horizon in the second and fourth panels. The first two panels are for the $\varphi_0 = 0.9$ cases and the last two panels are for the $\bar{V}_{,\varphi} = 1.458$ cases. Dashed lines are the values of φ from solving Eqs. (25) and (26).

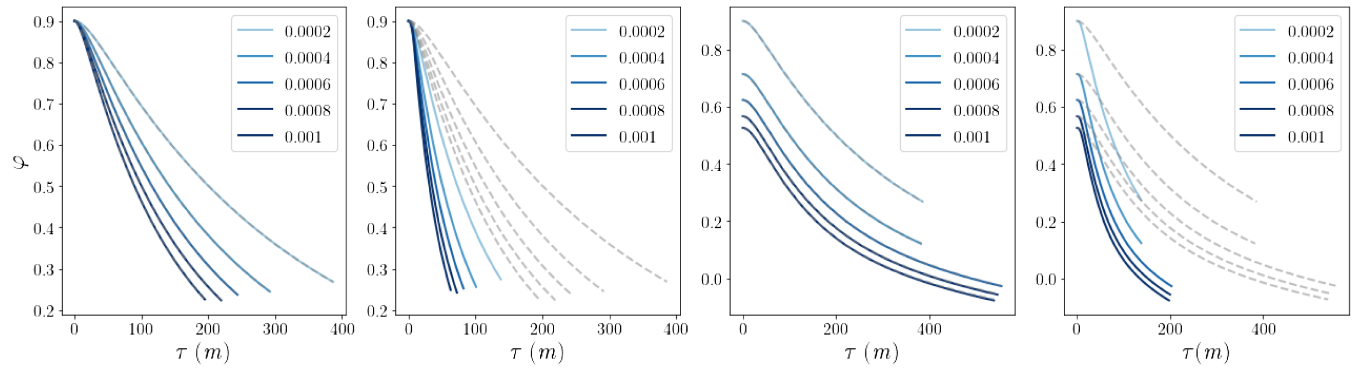

FIG. 5. Same as in Fig. 4, but as a function of proper time.

of proper time. Far from the BH, proper and coordinate time are the same since $\alpha \approx 1$.

For the type of potential we are considering, namely, $V = \lambda\varphi^4/4$, there is a rescaling that effectively eliminates λ. From the evolution equations (19) and (20) for the scalar field, this rescaling is $x^a \to \sqrt{\lambda}x^a$, $\Pi \to \Pi/\sqrt{\lambda}$, and $K \to K/\sqrt{\lambda}$. Figures 6 and 7 are the same as Figs. 4 and 5, respectively, under this rescaling.

VI. HORIZON AREA BALANCE LAW

According to the first law of BH dynamics, the area of the horizon of a BH in a nonequilibrium situation always increases. The dynamical horizon framework developed by Ashtekar and collaborators provides an expression relating the changes in the area of a BH to the fluxes across its dynamical horizon [81]. We will briefly summarize the expression and demonstrate that the outcome of our simulations satisfies such a balance law.

A dynamical horizon H is the world tube of marginally trapped surfaces or apparent horizons that we will label by S. H is foliated by S, and S is embedded in the spacelike hypersurface Σ used in the $3 + 1$ decomposition to solve the Einstein equations. With the unit timelike normal n^a to Σ and the unit spacelike normal s^a to S within Σ, the following outgoing l^a_Σ and ingoing k^a_Σ null vectors can be constructed:

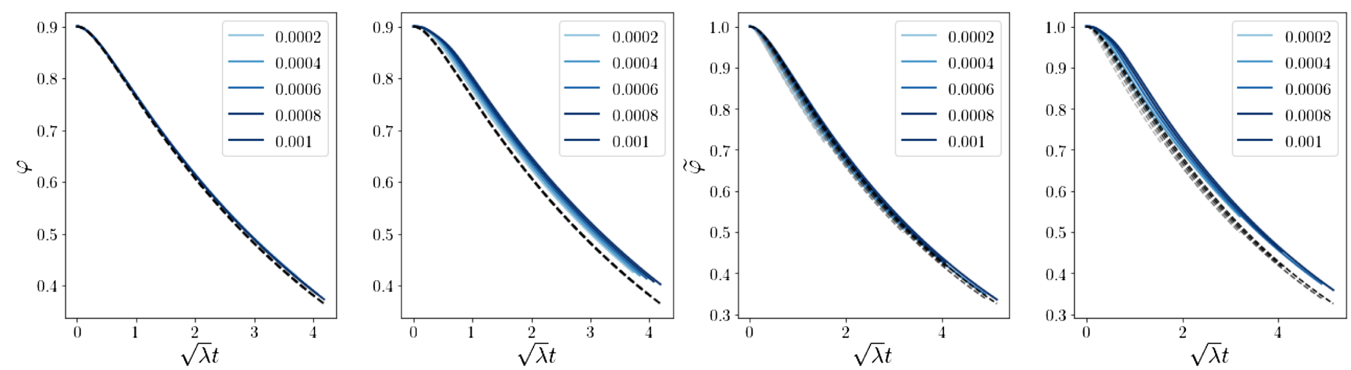

FIG. 6. Same as Fig. 4, but under the $t \to \sqrt{\lambda}t$. In the last two panels, φ has been normalized to its initial value.

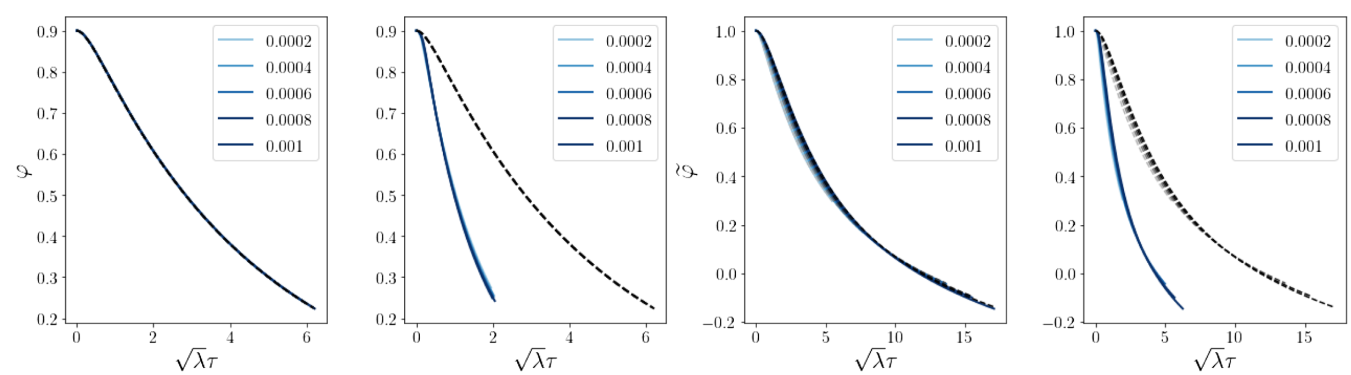

FIG. 7. Same as Fig. 5, but under the $t \to \sqrt{\lambda}t$. In the last two panels, φ has been normalized to its initial value.

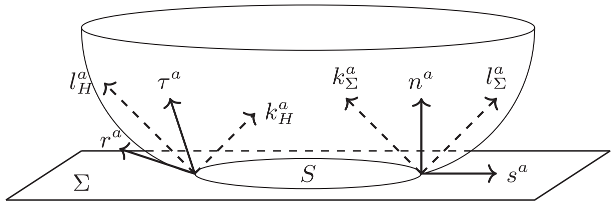

FIG. 8. Σ is the spacelike hypersurface used in the $3+1$ decomposition of the Einstein equations. S is the apparent horizon. n^a is timelike unit normal to Σ, and s^a is the spacelike unit normal to S in Σ. l_Σ^a and n_Σ^a are null vectors relative to n^a and s^a. H is the dynamical horizon, a spacelike hypersurface with timelike unit normal τ^a and a spacelike unit normal r^a normal to S in H. l_H^a and k_H^a are null vectors relative to τ^a and r_a.

$$l_\Sigma^a = \frac{1}{\sqrt{2}}(n^a + s^a), \tag{28}$$

$$k_\Sigma^a = \frac{1}{\sqrt{2}}(n^a - s^a). \tag{29}$$

The vectors n^a and s^a in terms of these null vectors are given by

$$n^a = \frac{1}{\sqrt{2}}(l_\Sigma^a + k_\Sigma^a), \tag{30}$$

$$s^a = \frac{1}{\sqrt{2}}(l_\Sigma^a - k_\Sigma^a). \tag{31}$$

Figure 8 provides a pictorial representation of the setup.

The expansion of l_Σ^a and k_Σ^a is given by

$$\Theta_{(l_\Sigma)} = h^{ab}\nabla_a l_b^\Sigma, \tag{32}$$

$$\Theta_{(k_\Sigma)} = h^{ab}\nabla_a k_b^\Sigma, \tag{33}$$

respectively, with

$$h_{ab} = g_{ab} + k_a^\Sigma l_b^\Sigma + l_a^\Sigma k_b^\Sigma = g_{ab} + n_a n_b - s_a s_b \tag{34}$$

the two-dimensional metric in S. A trapped surface is one in which $\Theta_{(l_\Sigma)} = 0$ and $\Theta_{(k_\Sigma)} < 0$. The outermost of these surfaces is the apparent horizon.

The dynamical horizon H is also a spacelike hypersurface. It has a unit timelike normal τ^a and unit spacelike normal r^a to S within H (see Fig. 8). With τ^a and r^a, the following null vectors can be constructed:

$$l_H^a = \sqrt{\frac{C}{2}}(\tau^a + r^a), \tag{35}$$

$$k_H^a = \frac{1}{\sqrt{2C}}(\tau^a - r^a), \tag{36}$$

with C a scalar field fixing the normalization of the null vectors. Equivalently,

$$\tau^a = \frac{1}{\sqrt{2C}}(l_H^a + Ck_H^a), \tag{37}$$

$$r^a = \frac{1}{\sqrt{2C}}(l_H^a - Ck_H^a). \tag{38}$$

Similarly, the expansion of l_H^a and k_H^a is given by

$$\Theta_{(l_H)} = h^{ab}\nabla_a l_b^H, \tag{39}$$

$$\Theta_{(k_H)} = h^{ab}\nabla_a k_b^H, \tag{40}$$

respectively, and the two-metric (34) in S takes the form

$$h_{ab} = g_{ab} + k_a^H l_b^H + l_a^H k_b^H = g_{ab} + \tau_a\tau_b - r_a r_b. \tag{41}$$

Here, again, for an apparent horizon $\Theta_{(l_H)} = 0$ and $\Theta_{(k_H)} < 0$.

Data from numerical relativity simulations are computed in Σ. On the other hand, the area increase law from the dynamical horizon framework is given in terms of quantities in H. Thus, we need to translate from one hypersurface to the other. The null vectors in Σ and H are related to each other via a boost transformation, which in the case of null vectors translates into a multiplicative factor f such that

$$l_H^a = f l_\Sigma^a \quad \text{and} \quad k_H^a = \frac{1}{f}k_\Sigma^a. \tag{42}$$

Notice that, with these transformations,

$$\Theta_{(l_H)} = f\Theta_{(l_\Sigma)} \quad \text{and} \quad \Theta_{(k_H)} = \frac{1}{f}\Theta_{(k_\Sigma)}, \tag{43}$$

and

$$r^a = \frac{1}{\sqrt{2C}}\left(f l_\Sigma^a - \frac{C}{f}k_\Sigma^a\right), \tag{44}$$

$$\tau^a = \frac{1}{\sqrt{2C}}\left(f l_\Sigma^a + \frac{C}{f}k_\Sigma^a\right). \tag{45}$$

Consider a horizon evolution vector field

$$\begin{aligned}\mathcal{U}^a &= Ur^a \\ &= \frac{U}{\sqrt{2C}}(l_H^a - Ck_H^a) \\ &= \frac{U}{\sqrt{2C}}\left(f l_\Sigma^a - \frac{C}{f}k_\Sigma^a\right).\end{aligned} \tag{46}$$

The vector field $\mathcal{U}^a$ is tangent to H, orthogonal to S, and generates a flow preserving the foliation in H. That is, $\mathcal{L}_{\mathcal{U}}\Theta_{(l_H)} = 0$, which implies that

$$\mathcal{L}_{l_H}\Theta_{(l_H)} - C\mathcal{L}_{k_H}\Theta_{(l_H)} = 0, \tag{47}$$

$$f^2\mathcal{L}_{l_\Sigma}\Theta_{(l_\Sigma)} - C\mathcal{L}_{k_\Sigma}\Theta_{(l_\Sigma)} = 0. \tag{48}$$

Thus,

$$\frac{C}{f^2} = \frac{\mathcal{L}_{l_\Sigma}\Theta_{(l_\Sigma)}}{\mathcal{L}_{k_\Sigma}\Theta_{(l_\Sigma)}}. \tag{49}$$

From the Raychaudhuri equation,

$$\begin{aligned}\mathcal{L}_{l_\Sigma}\Theta_{(l_\Sigma)} &= -\sigma^2 - R_{ab}l^a_\Sigma l^b_\Sigma \\ &= -8\pi T_{ab}l^a_\Sigma l^b_\Sigma,\end{aligned} \tag{50}$$

and from $G_{ab}l^a_\Sigma k^b_\Sigma = 8\pi T_{ab}l^a_\Sigma k^b_\Sigma$,

$$\begin{aligned}\mathcal{L}_{k_\Sigma}\Theta_{(l_\Sigma)} &= -\frac{\bar{\mathcal{R}}}{2} + 8\pi T_{ab}l^a_\Sigma k^b_\Sigma \\ &= -\frac{1}{R^2} + 8\pi T_{ab}l^a_\Sigma k^b_\Sigma,\end{aligned} \tag{51}$$

where $\bar{\mathcal{R}} = 2/R^2$ is the scalar curvature of the apparent horizon. Thus, substitution of Eqs. (50) and (51) into Eq. (49) yields

$$\frac{C}{f^2} = \frac{8\pi R^2 T_{ab}l^a_\Sigma l^b_\Sigma}{1 - 8\pi R^2 T_{ab}l^a_\Sigma k^b_\Sigma}. \tag{52}$$

From Eq. (5) for the stress-energy tensor, we have that

$$\begin{aligned}T_{ab}l^a_\Sigma l^b_\Sigma &= (l^a_\Sigma\nabla_a\varphi)^2 \\ &= \frac{1}{2}[(n^a + s^a)\nabla_a\varphi]^2 \\ &= \frac{1}{2}(-\Pi + s^i\partial_i\varphi)^2 \\ &= \frac{1}{2}\left[\mathring{\varphi} - \left(\frac{\beta^i}{\alpha} - s^i\right)\partial_i\varphi\right]^2 \\ &= \frac{1}{2}(\varphi')^2,\end{aligned} \tag{53}$$

where we have introduced the following definition:

$$\varphi' = \mathring{\varphi} - \left(\frac{\beta^i}{\alpha} - s^i\right)\partial_i\varphi. \tag{54}$$

Similarly,

$$\begin{aligned}T_{ab}l^a_\Sigma k^b_\Sigma &= l^a_\Sigma\nabla_a\varphi k^b_\Sigma\nabla_b\varphi + \frac{1}{2}\nabla_c\varphi\nabla^c\varphi + V \\ &= \frac{1}{2}\nabla_a\varphi\nabla_b\varphi(g^{ab} + l^a_\Sigma k^b_\Sigma + k^a_\Sigma l^b_\Sigma) + V \\ &= \frac{1}{2}h^{ab}\nabla_a\varphi\nabla_b\phi + V = V,\end{aligned} \tag{55}$$

where in the last step, we used that the projection of the gradients of ϕ on S vanishes because of the spherical symmetry. With Eqs. (53) and (55), Eq. (52) becomes

$$\frac{C}{f^2} = \frac{4\pi R^2(\varphi')^2}{1 - 8\pi R^2 V}. \tag{56}$$

The dynamical horizon framework [81] tells us that the area increase law reads

$$\frac{1}{2}\int dR = \mathcal{F}^{(\mathrm{m})} + \mathcal{F}^{(\mathrm{g})}. \tag{57}$$

The irreducible mass of the BH is obtained from $M = R/2 = \sqrt{A/16\pi}$. In Eq. (57),

$$\mathcal{F}^{(\mathrm{m})} = \sqrt{2}\int_{\Delta H} T_{ab}\tau^a\xi^b_R d^3\mathcal{V} \tag{58}$$

is the flux of matter-energy associated with ξ^a_R, and

$$\mathcal{F}^{(\mathrm{g})} = \frac{1}{16\pi}\int_{\Delta H} N_R(\sigma^2 + 2\zeta^2)d^3\mathcal{V} \tag{59}$$

is the energy carried by gravitational radiation. The vector field ξ^a_R is given by $\xi^a_R = N_R l^a_H$ with $N_R = |\partial R|_H$ a lapse function. $\sigma^2 = \sigma^{ab}\sigma_{ab}$ is the shear and $\zeta^2 = \zeta^a\zeta_a$ with $\zeta^a = h^{ab}r^c\nabla_c l^H_b$. Because we are dealing with a spherically symmetric case, there is no gravitational radiation emitted; thus, $\mathcal{F}^{(\mathrm{g})} = 0$. Also, using $d^3\mathcal{V} = N_R^{-1}dRd^2\mathcal{V}$, one can rewrite $\mathcal{F}^{(\mathrm{m})}$ as

$$\begin{aligned}\mathcal{F}^{(\mathrm{m})} &= \sqrt{2}\int dR\oint T_{ab}\tau^a l^b_H d^2\mathcal{V} \\ &= \frac{1}{\sqrt{2}}\int 8\pi R^2 T_{ab}\tau^a l^b_H dR,\end{aligned} \tag{60}$$

where we used in the last step that our system is spherically symmetric. Next, we use τ^a from Eq. (45) and l^a_H from Eq. (42) and rewrite $\mathcal{F}^{(\mathrm{m})}$ as

$$\begin{aligned}\mathcal{F}^{(\mathrm{m})} &= \frac{1}{2}\int 8\pi R^2 T_{ab}\frac{1}{\sqrt{C}}\left(fl^a_\Sigma + \frac{C}{f}k^a_\Sigma\right)fl^b_\Sigma dR \\ &= \frac{1}{2}\int\sqrt{C}(8\pi R^2 T_{ab}l^a_\Sigma l^b_\Sigma f^2/C \\ &\quad + 8\pi R^2 T_{ab}l^a_\Sigma k^b_\Sigma)dR.\end{aligned} \tag{61}$$

Finally, if we use Eq. (52) for C/f^2, we get that

$$\mathcal{F}^{(\mathrm{m})} = \frac{1}{2}\int \sqrt{C}dR. \tag{62}$$

Therefore, a comparison with the area law (57) yields that the normalization field is $C = 1$.

VII. BLACK HOLE MASS GROWTH

Next, we derive the expression for the rate of area increase starting from

$$\mathcal{L}_{\mathcal{U}} \ln \sqrt{h} = h^{ab}\nabla_a \mathcal{U}_b, \tag{63}$$

where h is the determinant of the metric h_{ab} in S. From Eq. (46), we have that

$$\begin{aligned}\mathcal{L}_{\mathcal{U}} \ln \sqrt{h} &= \frac{U}{\sqrt{2}}\left(f h^{ab}\nabla_a l_b^{\Sigma} - \frac{1}{f} h^{ab}\nabla_a k_b^{\Sigma}\right)\\ &= \frac{U}{\sqrt{2}}\left(f\Theta_{(l_\Sigma)} - \frac{1}{f}\Theta_{(k_\Sigma)}\right)\\ &= -\frac{U}{\sqrt{2}f}\Theta_{(k_\Sigma)}.\end{aligned} \tag{64}$$

Thus,

$$\mathcal{L}_{\mathcal{U}}\sqrt{h} = -\frac{U}{\sqrt{2}f}\Theta_{(k_\Sigma)}\sqrt{h}. \tag{65}$$

The area element in S is $\sqrt{h}d^2\Omega$. Therefore,

$$\begin{aligned}\mathcal{L}_{\mathcal{U}}\int_S \sqrt{h}d^2\Omega &= -\int_S \frac{U}{\sqrt{2}f}\Theta_{(k_\Sigma)}\sqrt{h}d^2\Omega,\\ \mathcal{L}_{\mathcal{U}}R^2 &= -R^2\frac{U}{\sqrt{2}f}\Theta_{(k_\Sigma)},\\ \mathcal{L}_{\mathcal{U}}R &= -\frac{R}{\sqrt{2}}\frac{U}{2f}\Theta_{(k_\Sigma)},\end{aligned} \tag{66}$$

where in the second-to-last equation, we used the spherical symmetry of our problem, and the expression is evaluated at S.

It is always possible to write $\mathcal{U}^a = \alpha(n^a + v s^a)$ where v is the coordinate velocity of the apparent horizon in Σ (see Fig. 9). On the other hand, from Eq. (47), we have that

$$\begin{aligned}\mathcal{U}^a &= \frac{U}{\sqrt{2}}\left(f l_\Sigma^a - \frac{1}{f}k_\Sigma^a\right)\\ &= \frac{U}{2}\left[f(n^a + s^a) - \frac{1}{f}(n^a - s^a)\right]\\ &= \frac{Uf}{2}\left[\left(1 - \frac{1}{f^2}\right)n^a + \left(1 + \frac{1}{f^2}\right)s^a\right].\end{aligned} \tag{67}$$

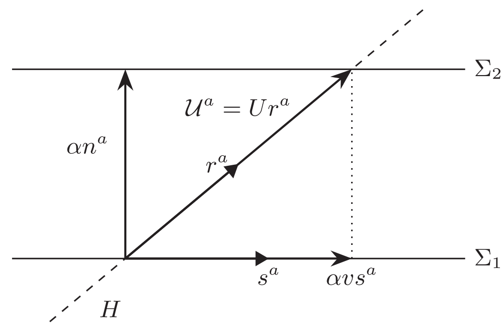

FIG. 9. Pictorial representation of the vector $\mathcal{U}^a$ relative to the hypersurfaces Σ and the dynamical horizon H.

Comparing the above expression with $\mathcal{U}^a = \alpha(n^a + v s^a)$ yields

$$\alpha = \frac{Uf}{2}\left(1 - \frac{1}{f^2}\right), \tag{68}$$

$$\alpha v = \frac{Uf}{2}\left(1 + \frac{1}{f^2}\right). \tag{69}$$

With Eq. (68), one can eliminate U from Eq. (66) and get

$$\mathcal{L}_{\mathcal{U}}R = -\frac{R}{\sqrt{2}}\alpha\Theta_{(k_\Sigma)}\frac{1}{f^2}\left(1 - \frac{1}{f^2}\right)^{-1}. \tag{70}$$

Substituting Eq. (52) into this expression, we get that

$$\begin{aligned}\mathcal{L}_{\mathcal{U}}R &= -\frac{R}{\sqrt{2}}\alpha\Theta_{(k_\Sigma)}\\ &\quad\times\left(\frac{8\pi R^2 T_{ab}l_\Sigma^a l_\Sigma^b}{1 - 8\pi R^2 T_{ab}l_\Sigma^a l_\Sigma^b - 8\pi R^2 T_{ab} l_\Sigma^a k_\Sigma^b}\right),\end{aligned} \tag{71}$$

or for our particular case

$$\mathcal{L}_{\mathcal{U}}R = -\frac{\sqrt{8}\pi\alpha\Theta_{(k_\Sigma)}R^3\varphi'^2}{1 - 8\pi R^2[\frac{1}{2}(\varphi')^2 + V]}. \tag{72}$$

With $t^a = \alpha n^a + \beta^a$, the vector field $\mathcal{U}^a = \alpha(n^a + v s^a)$ can be rewritten as $\mathcal{U}^a = t^a - \beta^a + \alpha v s^a$. Thus,

$$\begin{aligned}\mathcal{L}_{\mathcal{U}}R &= \mathcal{U}^a\nabla_a R\\ &= t^a\nabla_a R + (\alpha v s^a - \beta^a)\nabla_a R\\ &= \dot{R},\end{aligned} \tag{73}$$

where we have used that the BH areal radius is independent of the spatial coordinates in Σ. Finally,

$$\dot{R} = -\frac{\sqrt{8}\pi\alpha\Theta_{(k_\Sigma)}R^3\varphi'^2}{1 - 8\pi R^2[\frac{1}{2}\varphi'^2 + V]}, \tag{74}$$

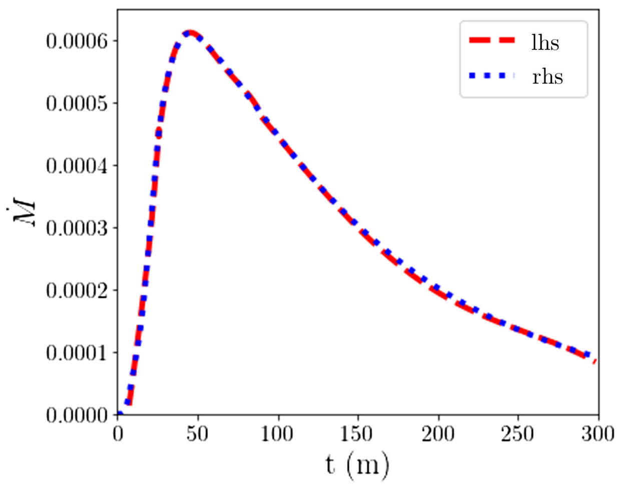

FIG. 10. BH mass growth rate as a function of time; (left) $\{\bar{\lambda}, \varphi_0\} = \{4, 0.714\}$ and (right) $\{4, 0.9\}$. The red dashed line shows the growth rate obtained from the area of the apparent horizon in the simulation, and the blue dotted line was obtained by directly substituting numerical data into Eq. (75).

or in terms of the BH mass

$$\dot{M} = -\frac{8\sqrt{2}\pi\alpha\Theta_{(k_\Sigma)}M^3\varphi'^2}{1 - 32\pi M^2[\frac{1}{2}\varphi'^2 + V]}. \tag{75}$$

As in both [59,61], we find that $\dot{M} \propto \dot{\varphi}^2$ since $\varphi' \propto \dot{\varphi}$. These studies also find that $\dot{M} \propto M^2$, similar to the standard Bondi accretion rate. Formula (75), on the other hand, seems to imply that $\dot{M} \propto M^3$, as in the study in Ref. [63]. However, we found that, as with the Schwarzschik-Vaidya metrics [81], $\Theta_{(k_\Sigma)} = -\epsilon/M$, with $\epsilon \approx \mathcal{O}(1)$; thus, $\dot{M} \propto M^2$.

To check the correctness of the mass growth rate as given by Eq. (75), we show in Figs. 10 and 11 with red dashed lines $\dot{M}$ calculated from the area of the apparent horizon and as a blue dotted line $\dot{M}$ calculated from substituting numerical data into the rhs of Eq. (75), demonstrating an explicit agreement. We recall that we start the simulation with a constant scalar field. The accretion rate peaks when the system enters the "steady" accretion.

Figures 12 and 13 show the BH mass growth rate as a function of time. In Fig. 12, the left panel is for $\varphi_0 = 0.9$ cases, and the right panel is for $\bar{V}_{,\varphi} = 1.458$ cases. Plots were created via Eq. (75). For the $\varphi_0 = 0.9$ cases in the left panel, the accretion rate increases with λ since the steepness of the potential is determined by λ and thus the larger value of φ'. In the right panel, we have the $\bar{V}_{,\varphi} = 1.458$ cases, namely, the situations for which the scalar field initially experiences the same force. The main difference here is that $\dot{M}$ decays faster as one increases λ; the larger the value of λ,

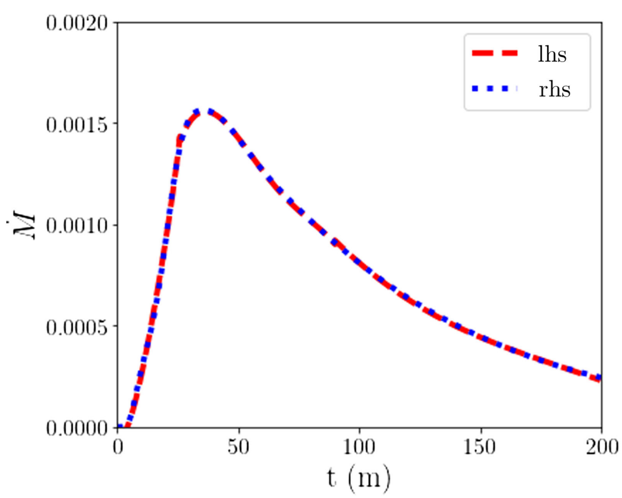

FIG. 11. BH mass growth rate as a function of time; (left) $\{\bar{\lambda}, \varphi_0\} = \{8, 0.526\}$ and (right) $\{8, 0.9\}$. The red dashed line shows the growth rate obtained from the area of the apparent horizon in the simulation, and the blue dotted line was obtained by directly substituting numerical data into Eq. (75).

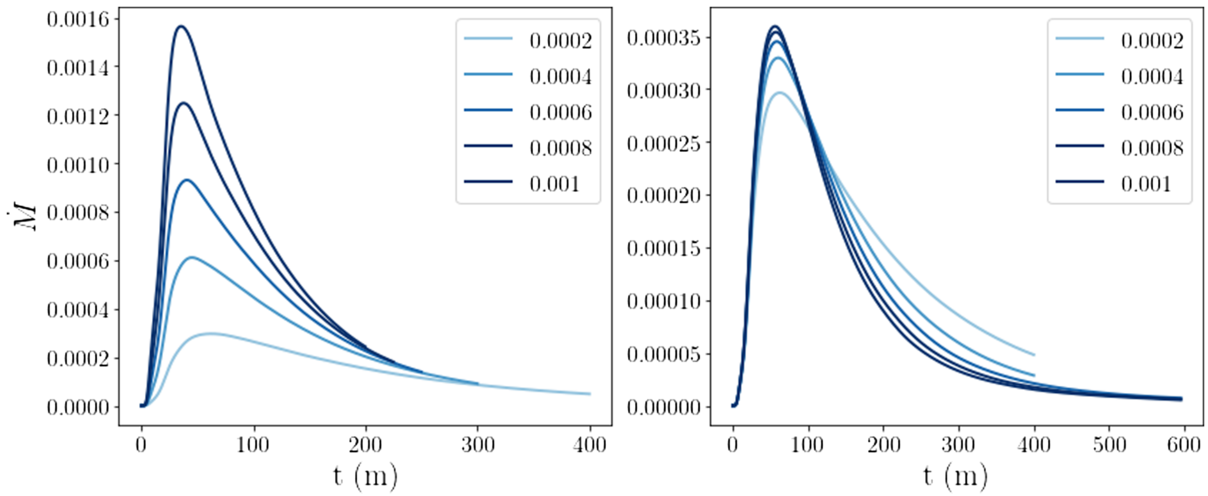

FIG. 12. BH mass growth rate as a function of time. Left: $\varphi_0 = 0.9$ cases. Right: $\bar{V}_{,\varphi} = 1.458$ cases. Plots were created via Eq. (75).

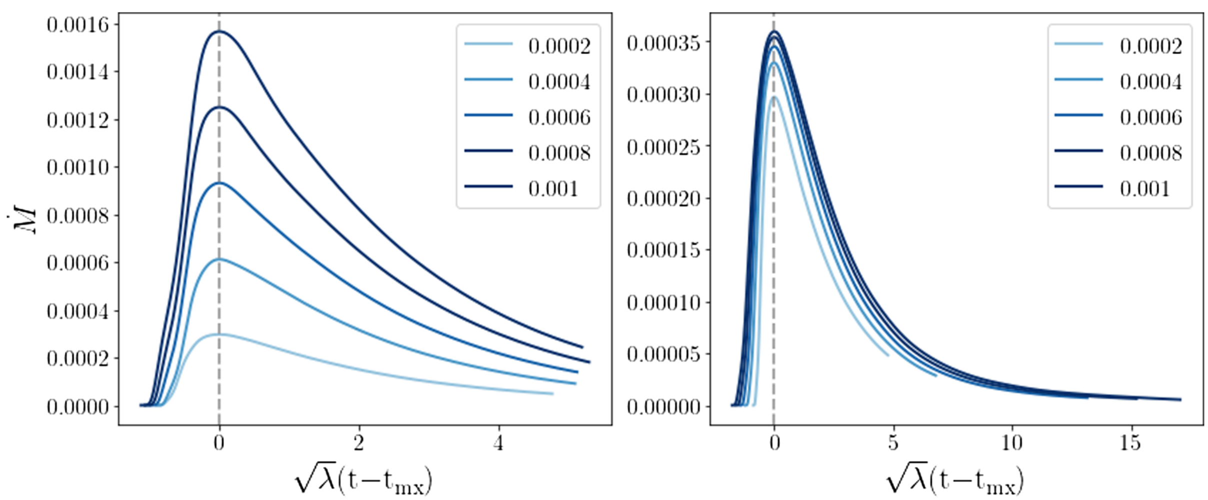

FIG. 13. Same as Fig. 12, but rescaling the axis by a factor $\sqrt{\lambda}$.

the steeper the potential, and the scalar field reaches the bottom of the potential faster. Figure 13 is the same as Fig. 12, but rescaling the time by a factor $\sqrt{\lambda}$ with the time shifted such that the maxima of $\dot{M}$ are aligned. Since the rescaling factors out the λ dependence, as expected, the cases with $\bar{V}_{,\varphi} = 1.458$ align with each other since the scalar field experiences the same initial force initially.

Figures 14 and 15 show the BH mass growth computed from the area of the apparent horizon as a function of time. In Fig. 14, the left panel is for the case $\varphi_0 = 0.9$, while the right panel is for the case $\bar{V}_{,\varphi} = 5.832$. Figure 15 is the same as Fig. 14, but rescaling the axis by a factor $\sqrt{\lambda}$.

To gain a better understanding of the BH mass growth formula as given by Eq. (75), we will approximate

$$\varphi' = \mathring{\varphi} - \left(\frac{\beta^i}{\alpha} - s^i\right)\partial_i\varphi \approx \mathring{\varphi}, \tag{76}$$

since, as seen in Sec. V, the scalar field does not vary much across the computational domain. Therefore, Eq. (75) becomes

$$\dot{M} \approx \frac{8\sqrt{2}\pi M^2\dot{\varphi}^2}{1 - 32\pi M^2[\frac{1}{2}\dot{\varphi}^2 + V]}, \tag{77}$$

where we have also used $\Theta_{(k_\Sigma)} \approx -M^{-1}$ and $\alpha \approx 1$. In addition, our simulations fall under the slow-roll regime in which $\dot{\varphi}^2/2 \ll V$. Therefore,

$$\dot{M} \approx \frac{8\sqrt{2}\pi M^2\dot{\varphi}^2}{1 - 32\pi M^2 V}. \tag{78}$$

Finally, our setup is such that $32\pi M^2 V \ll 1$ and thus

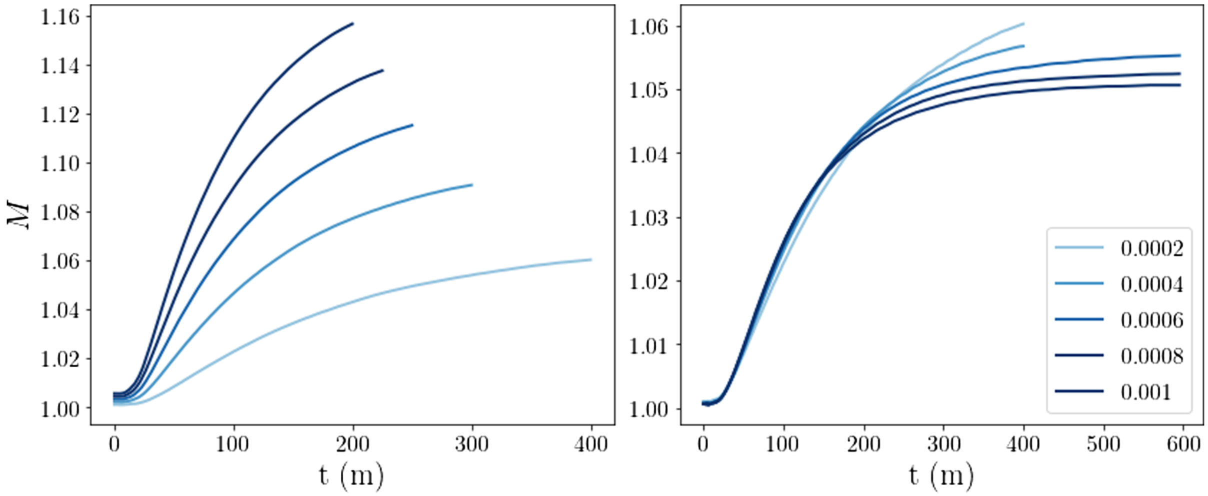

FIG. 14. BH mass growth computed from the area of the apparent horizon as a function of time. Left: the case $\varphi_0 = 0.9$. Right: the case $\bar{V}'(\varphi_0) = 5.832$.

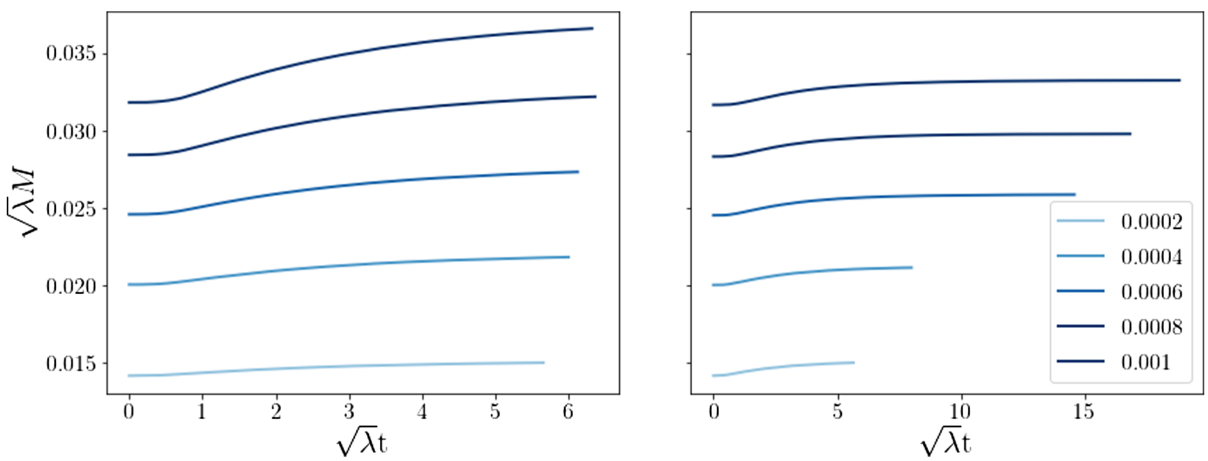

FIG. 15. Same as Fig. 14, but rescaling the time by a factor $\sqrt{\lambda}$.

$$\dot{M} \approx 8\sqrt{2}\pi M^2 \dot{\varphi}^2. \tag{79}$$

Under the slow-roll approximation, Eqs. (25) and (26) take the form

$$H^2 = \frac{8\pi}{3} V, \tag{80}$$

$$3H\dot{\varphi} = -V_{,\varphi}. \tag{81}$$

With our potential $V = \lambda\varphi^4/4$, solutions to Eqs. (80) and (81) yield

$$\dot{\varphi} = -\sqrt{\frac{\lambda}{6\pi}}\varphi_* \exp\left[-\sqrt{\frac{\lambda}{6\pi}}(t - t_*)\right], \tag{82}$$

where t_* and φ_* are the time and value of the scalar field when the system enters the slow-roll regime. Substitution of (82) into Eq. (79) yields

$$\frac{1}{M} = \frac{1}{M_*} - \frac{1}{\hat{M}}\left\{1 - \exp\left[-\sqrt{\frac{2\lambda}{3\pi}}(t - t_*)\right]\right\}, \tag{83}$$

where

$$\frac{1}{\hat{M}} \equiv \sqrt{\frac{16\pi\lambda}{3}}\varphi_*^2. \tag{84}$$

For $t \gg t_*$, Eq. (83) becomes

$$\frac{M_*}{M} = 1 - \frac{M_*}{\hat{M}}. \tag{85}$$

To grow a BH with mass M_* by a factor of $\xi = M/M_*$ would require

$$\xi = \left(1 - \frac{M_*}{\hat{M}}\right)^{-1}. \tag{86}$$

For the values used in the present work of $\lambda \sim 10^{-4} m^{-2}$, $\varphi_* \sim 1$, and $M_* \sim 1$ m, one has that $M_*/\hat{M} \sim 4 \times 10^{-2}$, which yields $\xi \sim 1.04$, an estimate consistent with the results found in the previous section.

VIII. CONCLUSIONS

We have conducted a numerical relativity study of the accretion properties of a nonspinning black hole in a cosmology driven by a scalar field. Because the space-time is not asymptotically flat, we introduced modifications to the moving-puncture gauge condition to be able to function in cosmological space-times. We considered a scalar field with potential $V = \lambda\varphi^4/4$ and varied the parameter λ as well as the initial conditions for the scalar field. We derived the black hole mass growth formula for these cosmological scenarios using the dynamical horizon framework. We verified that the results from the simulations satisfy this mass growth formula. As with perturbative studies, we found that the accretion rate $\dot{M} \propto M^2$, with M the mass of the black hole, and that $\dot{M} \propto \dot{\varphi}^2$. What was not anticipated was that the dynamics of the scalar field in the neighborhood of the black hole is not significantly different from the behavior of the field far away from the hole. We found situations in which the black hole can grow ~15% of its initial mass before the scalar field reaches the bottom of its potential. The next step is to investigate BH scalar accretion for BHs with spin and linear momentum.

We have investigated BH scalar accretion in a simple setup. The next step is to consider more complex scalar field dynamics that could potentially yield larger accretion rates and provide a potential scenario for the growth of seeds for massive BHs. Another scenario we are considering is the merger of BBHs in these environments.

ACKNOWLEDGMENTS

This work is supported by NSF Grants No. PHY-2411068 and No. PHY-2207780.

DATA AVAILABILITY

The data that support the findings of this article are not publicly available upon publication because it is not technically feasible and/or the cost of preparing, depositing, and hosting the data would be prohibitive within the terms of this research project. The data are available from the authors upon reasonable request.

[1] B. P. Abbott *et al.*, Tests of general relativity with GW150914, Phys. Rev. Lett. **116**, 221101 (2016); **121**, 129902(E) (2018).

[2] R. Abbott *et al.*, Tests of general relativity with binary black holes from the second LIGO-Virgo gravitational-wave transient catalog, Phys. Rev. D **103**, 122002 (2021).

[3] B. P. Abbott *et al.*, Tests of general relativity with the binary black hole signals from the LIGO-Virgo catalog GWTC-1, Phys. Rev. D **100**, 104036 (2019).

[4] Virgo, LIGO Scientific, and KAGRA Collaborations, Tests of general relativity with GWTC-3, arXiv:2112.06861.,

[5] Joseph M. Fedrow, Christian D. Ott, Ulrich Sperhake, Jonathan Blackman, Roland Haas, Christian Reisswig, and Antonio De Felice, Gravitational waves from binary black hole mergers inside stars, Phys. Rev. Lett. **119**, 171103 (2017).

[6] Alexandre Toubiana, Laura Sberna, Andrea Caputo, Giulia Cusin, Sylvain Marsat, Karan Jani, Stanislav Babak, Enrico Barausse, Chiara Caprini, Paolo Pani, Alberto Sesana, and Nicola Tamanini, Detectable environmental effects in GW190521-like black-hole binaries with LISA, Phys. Rev. Lett. **126**, 101105 (2021).

[7] Emanuele Berti *et al.*, Testing general relativity with present and future astrophysical observations, Classical Quantum Gravity **32**, 243001 (2015).

[8] Nicolás Yunes, Kent Yagi, and Frans Pretorius, Theoretical physics implications of the binary black-hole mergers GW150914 and GW151226, Phys. Rev. D **94**, 084002 (2016).

[9] Juan Calderón Bustillo, Nicolas Sanchis-Gual, Samson H. W. Leong, Koustav Chandra, Alejandro Torres-Forne, Jose A. Font, Carlos Herdeiro, Eugen Radu, Isaac C. F. Wong, and T. G. F. Li, Searching for vector boson-star mergers within LIGO-Virgo intermediate-mass black-hole merger candidates, Phys. Rev. D **108**, 123020 (2023).

[10] Juan Calderón Bustillo, Nicolas Sanchis-Gual, Alejandro Torres-Forné, José A. Font, Avi Vajpeyi, Rory Smith, Carlos Herdeiro, Eugen Radu, and Samson H. W. Leong, GW190521 as a merger of proca stars: A potential new vector boson of 8.7×10^{-13} eV, Phys. Rev. Lett. **126**, 081101 (2021).

[11] Matthew J. Graham, Barry McKernan, K. E. Saavik Ford, Daniel Stern, S. G. Djorgovski, Michael Coughlin, Kevin B. Burdge, Eric C. Bellm, George Helou, Ashish A. Mahabal, Frank J. Masci, Josiah Purdum, Philippe Rosnet, and Ben Rusholme, A light in the dark: Searching for electromagnetic counterparts to black hole–black hole mergers in LIGO/Virgo O3 with the Zwicky Transient Facility, Astrophys. J. **942**, 99 (2023).

[12] Connar Rowan, Tjarda Boekholt, Bence Kocsis, and Zoltán Haiman, Black hole binary formation in AGN discs: From

isolation to merger, Mon. Not. R. Astron. Soc. **524**, 2770 (2023).
[13] Hiromichi Tagawa, Zoltán Haiman, and Bence Kocsis, Formation and evolution of compact-object binaries in AGN disks, Astrophys. J. **898**, 25 (2020).
[14] K. E. Saavik Ford and Barry McKernan, Binary black hole merger rates in AGN discs versus nuclear star clusters: Loud beats quiet, Mon. Not. R. Astron. Soc. **517**, 5827 (2022).
[15] Avi Vajpeyi, Eric Thrane, Rory Smith, Barry McKernan, and K. E. Saavik Ford, Measuring the properties of active galactic nuclei disks with gravitational waves, Astrophys. J. **931**, 82 (2022).
[16] M. Gröbner, W. Ishibashi, S. Tiwari, M. Haney, and P. Jetzer, Binary black hole mergers in AGN accretion discs: Gravitational wave rate density estimates, Astron. Astrophys. **638**, A119 (2020).
[17] Barry McKernan, K. E. Saavik Ford, J. Bellovary, N. W. C. Leigh, Z. Haiman, B. Kocsis, W. Lyra, M.-M. Mac Low, B. Metzger, M. O'Dowd, S. Endlich, and D. J. Rosen, Constraining stellar-mass black hole mergers in AGN disks detectable with LIGO, Astrophys. J. **866**, 66 (2018).
[18] Abid Khan, Vasileios Paschalidis, Milton Ruiz, and Stuart L. Shapiro, Disks around merging binary black holes: From GW150914 to supermassive black holes, Phys. Rev. D **97**, 044036 (2018).
[19] Nicolás Yunes, Bence Kocsis, Abraham Loeb, and Zoltán Haiman, Imprint of accretion disk-induced migration on gravitational waves from extreme mass ratio inspirals, Phys. Rev. Lett. **107**, 171103 (2011).
[20] I. D. Novikov and K. S. Thorne, Astrophysics and black holes, in *Les Houches Summer School of Theoretical Physics: Black Holes* (Gordon and Breach, Science Publishers, Inc, New York City, US, 1973), pp. 343–550.
[21] Laura Sberna, Stanislav Babak, Sylvain Marsat, Andrea Caputo, Giulia Cusin, Alexandre Toubiana, Enrico Barausse, Chiara Caprini, Tito Dal Canton, Alberto Sesana, and Nicola Tamanini, Observing GW190521-like binary black holes and their environment with LISA, Phys. Rev. D **106**, 064056 (2022).
[22] Vitor Cardoso, Kyriakos Destounis, Francisco Duque, Rodrigo Panosso Macedo, and Andrea Maselli, Black holes in galaxies: Environmental impact on gravitational-wave generation and propagation, Phys. Rev. D **105**, L061501 (2022).
[23] Vitor Cardoso and Andrea Maselli, Constraints on the astrophysical environment of binaries with gravitational-wave observations, Astron. Astrophys. **644**, A147 (2020).
[24] Enrico Barausse, Vitor Cardoso, and Paolo Pani, Can environmental effects spoil precision gravitational-wave astrophysics?, Phys. Rev. D **89**, 104059 (2014).
[25] Vitor Cardoso, Kyriakos Destounis, Francisco Duque, Rodrigo Panosso Macedo, and Andrea Maselli, Gravitational waves from extreme-mass-ratio systems in astrophysical environments, Phys. Rev. Lett. **129**, 241103 (2022).
[26] Yu-Peng Zhang, Miguel Gracia-Linares, Pablo Laguna, Deirdre Shoemaker, and Yu-Xiao Liu, Gravitational recoil from binary black hole mergers in scalar field clouds, Phys. Rev. D **107**, 044039 (2023).
[27] Caio F. B. Macedo, Paolo Pani, Vitor Cardoso, and Luís C. B. Crispino, Into the lair: Gravitational-wave signatures of dark matter, Astrophys. J. **774**, 48 (2013).
[28] Nicolás Yunes, Paolo Pani, and Vitor Cardoso, Gravitational waves from quasicircular extreme mass-ratio inspirals as probes of scalar-tensor theories, Phys. Rev. D **85**, 102003 (2012).
[29] Emanuele Berti, Vitor Cardoso, Leonardo Gualtieri, Michael Horbatsch, and Ulrich Sperhake, Numerical simulations of single and binary black holes in scalar-tensor theories: Circumventing the no-hair theorem, Phys. Rev. D **87**, 124020 (2013).
[30] James Healy, Tanja Bode, Roland Haas, Enrique Pazos, Pablo Laguna, Deirdre M. Shoemaker, and Nicolás Yunes, Late inspiral and merger of binary black holes in scalar–tensor theories of gravity, Classical Quantum Gravity **29**, 232002 (2012).
[31] Kent Yagi and Takahiro Tanaka, Constraining alternative theories of gravity by gravitational waves from precessing eccentric compact binaries with LISA, Phys. Rev. D **81**, 064008 (2010).
[32] Zhoujian Cao, Pablo Galaviz, and Li-Fang Li, Binary black hole mergers in $f(r)$ theory, Phys. Rev. D **87**, 104029 (2013).
[33] Eric W. Hirschmann, Luis Lehner, Steven L. Liebling, and Carlos Palenzuela, Black hole dynamics in Einstein-Maxwell-Dilaton theory, Phys. Rev. D **97**, 064032 (2018).
[34] Qing Yang, Li-Wei Ji, Bin Hu, Zhou-Jian Cao, and Rong-Gen Cai, An axion-like scalar field environment effect on binary black hole merger, Res. Astron. Astrophys. **18**, 065 (2018).
[35] Leong Khim Wong, Evolution of diffuse scalar clouds around binary black holes, Phys. Rev. D **101**, 124049 (2020).
[36] Alejandro Cruz-Osorio, F. Siddhartha Guzmán, and Fabio D. Lora-Clavijo, Scalar field dark matter: Behavior around black holes, J. Cosmol. Astropart. Phys. 06 (2011) 029.
[37] William E. East and Frans Pretorius, Superradiant instability and backreaction of massive vector fields around Kerr black holes, Phys. Rev. Lett. **119**, 041101 (2017).
[38] William E. East, Massive boson superradiant instability of black holes: Nonlinear growth, saturation, and gravitational radiation, Phys. Rev. Lett. **121**, 131104 (2018).
[39] Vitor Cardoso, Isabella P. Carucci, Paolo Pani, and Thomas P. Sotiriou, Matter around Kerr black holes in scalar-tensor theories: Scalarization and superradiant instability, Phys. Rev. D **88**, 044056 (2013).
[40] Jun Zhang and Huan Yang, Dynamic signatures of black hole binaries with superradiant clouds, Phys. Rev. D **101**, 043020 (2020).
[41] Leong Khim Wong, Carlos A. R. Herdeiro, and Eugen Radu, Constraining spontaneous black hole scalarization in scalar-tensor-gauss-bonnet theories with current gravitational-wave data, Phys. Rev. D **106**, 024008 (2022).
[42] Eloisa Bentivegna, Deirdre M. Shoemaker, Ian Hinder, and Frank Herrmann, Probing the binary black hole merger regime with scalar perturbations, Phys. Rev. D **77**, 124016 (2008).
[43] James Healy, Tanja Bode, Roland Haas, Enrique Pazos, Pablo Laguna, Deirdre M. Shoemaker, and Nicolás Yunes, Late inspiral and merger of binary black holes in scalar-tensor theories of gravity, Classical Quantum Gravity **29**, 232002 (2012).

[44] Emanuele Berti, Vitor Cardoso, Leonardo Gualtieri, Michael Horbatsch, and Ulrich Sperhake, Numerical simulations of single and binary black holes in scalar-tensor theories: Circumventing the no-hair theorem, Phys. Rev. D **87**, 124020 (2013).
[45] Zhoujian Cao, Pablo Galaviz, and Li-Fang Li, Binary black hole mergers in $f(R)$ theory, Phys. Rev. D **87**, 104029 (2013).
[46] Maria Okounkova, Leo C. Stein, Mark A. Scheel, and Daniel A. Hemberger, Numerical binary black hole mergers in dynamical Chern-Simons gravity: Scalar field, Phys. Rev. D **96**, 044020 (2017).
[47] Qing Yang, Li-Wei Ji, Bin Hu, Zhou-Jian Cao, and Rong-Gen Cai, An axion-like scalar field environment effect on binary black hole merger, Res. Astron. Astrophys. **18**, 065 (2018).
[48] Eric W. Hirschmann, Luis Lehner, Steven L. Liebling, and Carlos Palenzuela, Black hole dynamics in Einstein-Maxwell-Dilaton theory, Phys. Rev. D **97**, 064032 (2018).
[49] Helvi Witek, Leonardo Gualtieri, Paolo Pani, and Thomas P. Sotiriou, Black holes and binary mergers in scalar Gauss-Bonnet gravity: Scalar field dynamics, Phys. Rev. D **99**, 064035 (2019).
[50] David J. E. Marsh, Axion cosmology, Phys. Rep. **643**, 1 (2016).
[51] Robert V. Wagoner, Scalar tensor theory and gravitational waves, Phys. Rev. D **1**, 3209 (1970).
[52] Antonio De Felice and Shinji Tsujikawa, f(R) theories, Living Rev. Relativity **13**, 3 (2010).
[53] Thomas P. Sotiriou and Valerio Faraoni, f(R) theories of gravity, Rev. Mod. Phys. **82**, 451 (2010).
[54] Abhirup Ghosh *et al.*, Testing general relativity using gravitational wave signals from the inspiral, merger and ringdown of binary black holes, Classical Quantum Gravity **35**, 014002 (2017).
[55] Peter T. H. Pang, Juan Calderón Bustillo, Yifan Wang, and Tjonnie G. F. Li, Potential observations of false deviations from general relativity in gravitational wave signals from binary black holes, Phys. Rev. D **98**, 024019 (2018).
[56] Dina Traykova, Katy Clough, Thomas Helfer, Emanuele Berti, Pedro G. Ferreira, and Lam Hui, Dynamical friction from scalar dark matter in the relativistic regime, Phys. Rev. D **104**, 103014 (2021).
[57] Rodrigo Vicente and Vitor Cardoso, Dynamical friction of black holes in ultralight dark matter, Phys. Rev. D **105**, 083008 (2022).
[58] James Healy, Tanja Bode, Roland Haas, Enrique Pazos, Pablo Laguna, Deirdre M. Shoemaker, and Nicolás Yunes, Late inspiral and merger of binary black holes in scalar–tensor theories of gravity, Classical Quantum Gravity **29**, 232002 (2012).
[59] Ruth Gregory, David Kastor, and Jennie Traschen, Evolving black holes in inflation, Classical Quantum Gravity **35**, 155008 (2018).
[60] Lewis Croney, Ruth Gregory, and Sam Patrick, Ultra slow-roll with a black hole, J. Cosmol. Astropart. Phys. 01 (2025) 096.
[61] Marco de Cesare and Roberto Oliveri, Evolving black hole with scalar field accretion, Phys. Rev. D **106**, 044033 (2022).
[62] Vitor Cardoso, Taishi Ikeda, Rodrigo Vicente, and Miguel Zilhão, Parasitic black holes: The swallowing of a fuzzy dark matter soliton, Phys. Rev. D **106**, L121302 (2022).
[63] Malik Almatwi, Interaction of a black hole with scalar field in cosmology background, Eur. Phys. J. C **84**, 845 (2024).
[64] Thomas W. Baumgarte and Stuart L. Shapiro, *Numerical Relativity: Solving Einstein's Equations on the Computer* (Cambridge University Press, Cambridge, England, 2010).
[65] A. Lichnerowicz, L'integration des équations relativistes et le problème des n corps, J. Math. Pures Appl. **23**, 37 (1944).
[66] James W. York, Gravitational degrees of freedom and the initial-value problem, Phys. Rev. Lett. **26**, 1656 (1971).
[67] James W. York, Role of conformal three-geometry in the dynamics of gravitation, Phys. Rev. Lett. **28**, 1082 (1972).
[68] Gregory B. Cook, Initial data for numerical relativity, Living Rev. Relativity **3**, 5 (2000).
[69] Jeffrey M. Bowen and James W. York, Time-asymmetric initial data for black holes and black-hole collisions, Phys. Rev. D **21**, 2047 (1980).
[70] Thomas W. Baumgarte and Stuart L. Shapiro, Numerical integration of Einstein's field equations, Phys. Rev. D **59**, 024007 (1998).
[71] Masaru Shibata and Takashi Nakamura, Evolution of three-dimensional gravitational waves: Harmonic slicing case, Phys. Rev. D **52**, 5428 (1995).
[72] M. Campanelli, C. O. Lousto, P. Marronetti, and Y. Zlochower, Accurate evolutions of orbiting black-hole binaries without excision, Phys. Rev. Lett. **96**, 111101 (2006).
[73] John G. Baker, Joan Centrella, Dae-Il Choi, Michael Koppitz, and James van Meter, Gravitational wave extraction from an inspiraling configuration of merging black holes, Phys. Rev. Lett. **96**, 111102 (2006).
[74] Tom Goodale, Gabrielle Allen, Gerd Lanfermann, Joan Masso, Thomas Radke, Edward Seidel, and John Shalf, The cactus framework and toolkit: Design and applications, in *VECPAVector and Parallel Processing R'2002, 5th International Conference* (Springer, Berlin, 2003).
[75] Sascha Husa, Ian Hinder, and Christiane Lechner, Kranc: A Mathematica application to generate numerical codes for tensorial evolution equations, Comput. Phys. Commun. **174**, 983 (2006).
[76] Roland Haas, Roman V. Shcherbakov, Tanja Bode, and Pablo Laguna, Tidal disruptions of white dwarfs from ultra-close encounters with intermediate-mass spinning black holes, Astrophys. J. **749**, 117 (2012).
[77] Christopher Evans, Pablo Laguna, and Michael Eracleous, Ultra-close encounters of stars with massive black holes: Tidal disruption events with prompt hyperaccretion, Astrophys. J. Lett. **805**, L19 (2015).
[78] Michael Clark and Pablo Laguna, Bowen-York-type initial data for binaries with neutron stars, Phys. Rev. D **94**, 064058 (2016).
[79] Karan Jani, James Healy, James A. Clark, Lionel London, Pablo Laguna, and Deirdre Shoemaker, Georgia tech catalog of gravitational waveforms, Classical Quantum Gravity **33**, 204001 (2016).
[80] Steven R. Brandt *et al.*, The EINSTEIN TOOLKIT: Open software for relativistic astrophysics, 10.5281/zenodo.15520463 (2025).
[81] Abhay Ashtekar and Badri Krishnan, Isolated and dynamical horizons and their applications, Living Rev. Relativity **7**, 10 (2004).